J. Fluid Mech. (2012), *vol.* 695, *pp.* 341–365. © Cambridge University Press 2012
doi:10.1017/jfm.2012.24

A multi-layer model for nonlinear internal wave propagation in shallow water

Philip L.-F. Liu[1,2]† **and Xiaoming Wang**[1,3]

[1] School of Civil and Environmental Engineering, Cornell University, Ithaca, NY 14853, USA

[2] Institute of Hydrological and Oceanic Sciences, National Central University, Jhongli, Taoyuan 32001, Taiwan

[3] GNS Science, Wairakei 3377, New Zealand

(Received 17 October 2010; revised 3 October 2011; accepted 7 January 2012; first published online 9 February 2012)

In this paper, a multi-layer model is developed for the purpose of studying nonlinear internal wave propagation in shallow water. The methodology employed in constructing the multi-layer model is similar to that used in deriving Boussinesq-type equations for surface gravity waves. It can also be viewed as an extension of the two-layer model developed by Choi & Camassa. The multi-layer model approximates the continuous density stratification by an N-layer fluid system in which a constant density is assumed in each layer. This allows the model to investigate higher-mode internal waves. Furthermore, the model is capable of simulating large-amplitude internal waves up to the breaking point. However, the model is limited by the assumption that the total water depth is shallow in comparison with the wavelength of interest. Furthermore, the vertical vorticity must vanish, while the horizontal vorticity components are weak. Numerical examples for strongly nonlinear waves are compared with laboratory data and other numerical studies in a two-layer fluid system. Good agreement is observed. The generation and propagation of mode-1 and mode-2 internal waves and their interactions with bottom topography are also investigated.

Key words: internal waves, shallow water flows, topographic effects

1. Introduction

Long internal waves are frequently observed in the oceanic environment (Farmer 1978; Liu 1988; Liu *et al.* 1998; Duda *et al.* 2004). Because of their strong vertical motions, internal waves make significant contributions to nutrient mixing, especially when they break in coastal regions (Sandstrom & Elliot 1984). Internal waves could also have negative impacts on offshore structures and their mooring systems, and the operation of submarine vehicles (Bole, Ebbesmeyer & Romea 1994; Apel *et al.* 1997). One of the main mechanisms of internal wave generation is through the interaction between tides and submarine topography, such as shelf edges, submarine ridges and sills. In the South China Sea, synthetic aperture radar (SAR) images from satellites clearly show the surface signatures of large-amplitude internal wave packets (with wavelengths varying from 500 m to 5 km), which are most likely generated by diurnal

† Email address for correspondence: Philip.liu@cornell.edu

https://doi.org/10.1017/jfm.2012.24 Published online by Cambridge University Press

tides over the shallow ridges (∼200–300 m deep) in the Luzon Strait and evolve into the South China Sea. These internal wave packets propagate over several hundred kilometres with speeds up to 2.0 m s^{-1} and finally reach the continental shelf of Southern China (Liu *et al.* 1998; Hsu, Liu & Liu 2000; Yang *et al.* 2004).

Numerous experimental and theoretical efforts have been made to study the characteristics of internal waves, including their generation, evolution and interactions with other waves and with bathymetric features. Equations of Korteweg–de Vries (KdV) type have played a key role in understanding the essential features of the observations (Lee & Beardsley 1974; Farmer 1978; Liu 1988; Grimshaw, Pelinovsky & Ploukhina 2002). However, their applications are limited to uni-directional wave propagation with the weakly nonlinear assumption.

Satellite images in the South China Sea clearly suggest strong two-dimensional wave–wave interactions and show complex wave patterns because of the reflection and refraction of internal waves by bathymetry and islands (Liu *et al.* 1998). To include the weak horizontally two-dimensional (H2D) effects, equations of Kadomtsev–Petviashvili (KP) type have been applied to situations such as wave propagation through a narrow channel (Tomasson & Melville 1992; Chen & Liu 1995), in which the spatial variation of the wave form in the transverse direction is small in comparison with that along the direction of wave propagation. Small (2001*a*,*b*) extended the application of KdV theory into a two-dimensional basin by coupling the classical ray theory and the KdV equations and studied the shoaling and refraction of internal solitary waves. To account for the full H2D effects, Choi & Camassa (1996) derived a set of weakly nonlinear equations for internal waves in a two-layer fluid system with a sharp interface dividing the flow field into two constant-density regions. Using a similar depth-integrating approach, a weakly nonlinear H2D model in a two-layer system was also derived by Lynett & Liu (2002) for internal waves propagating over a slowly varying bathymetry. Their model has been successfully implemented to study the evolution, refraction and reflection of internal waves in the South China Sea and the Strait of Gibraltar. The results, qualitatively, produce a fairly good match with the SAR observations.

Because of the relatively weak density stratification in the ocean, internal waves may attain a relatively large amplitude, which have been widely observed in the ocean (Stanton & Ostrovsky 1998). For example, in the South China Sea, an amplitude up to 165 m was observed in 340 m water depth with a background upper layer of ∼40 m (Duda *et al.* 2004). Thus, weakly nonlinear theory is not sufficient for the accurate description of internal waves of large amplitude. Recently, more advanced models in terms of a two-layer fluid system have been developed to include the strongly nonlinear effects (Choi & Camassa 1999; Jo & Choi 2002; Camassa *et al.* 2006). Most recently, Debsarma, Das & Kirby (2010) extended Choi & Camassa's (1999) two-layer model to include higher-order effects of frequency dispersion.

In a two-layer system, the pycnocline is ignored and is replaced by a density discontinuity. Consequently, two-layer models can only simulate the mode-1 internal waves and are not capable of describing higher-mode internal waves, which require a more complex description of the pycnocline. The higher-mode internal waves travel with slower speeds than that of the mode-1 internal wave and are usually generated through interaction of the mode-1 internal wave with bottom topography, the breaking of the mode-1 internal waves, the intrusion of fluid into the pycnocline, or forced by the barotropic tide. In both laboratory experiments and field measurements, mode-2 internal waves have been frequently observed (Kao & Pao 1980; Maxworthy

https://doi.org/10.1017/jfm.2012.24 Published online by Cambridge University Press

1980, 1983; Helfrich 1992; Huttemann & Hutter 2001; Duda *et al.* 2004; Yang *et al.* 2004; Vazquez *et al.* 2006).

In numerical studies, mode-2 waves can be generated either by density anomaly (Terez & Knio 1998; Chao *et al.* 2006) or by interactions between mode-1 waves and bottom obstacles (Vlasenko & Hutter 2001; Vlasenko & Alpers 2005). Two-dimensional Euler equations or Navier–Stokes equations on the vertical plane are usually implemented to study the generation and evolution of mode-2 waves with either continuous stratification (Evans & Ford 1996; Saffarinia & Kao 1996; Grue *et al.* 1997; Grue, Jensen & Rusas 1999; Huttemann & Hutter 2001; Vlasenko & Hutter 2001; Vlasenko & Alpers 2005; Chao *et al.* 2006) or a layered fluid system (Lamb 2000; Rusas & Grue 2002). Using a three-dimensional Navier–Stokes equation model, Chao *et al.* (2006) investigated the reflection and diffraction of mode-1 and mode-2 solitary internal waves by a circular island. Both mode-1 and mode-2 internal waves were generated by an initial density anomaly prescribed by a modal structure. However, these nonlinear equations are expensive to solve even for relatively simple situations in three dimensions. It is extremely difficult to employ these models for large-scale simulations. Consequently, studies using Euler equations have mostly been focusing on horizontally one-dimensional (vertical plane) problems.

Thus, there is a need to develop models that are accurate in capturing the essential dynamics in a physically realistic situation, yet simple enough to be applied efficiently for large-scale problems. Practically, continuous stratification in the water column can be approximated by a multi-layered fluid system, in which the water column is divided into the desired number of layers and within each layer the density is approximated as a constant. Consider the shallow-water environment, where the wavelength of the wave system is much longer than the water depth, and the layer thickness is also much smaller than the wavelength. The shallow-water wave approximation can then be implemented in each individual layer and the Euler equation can be integrated vertically through the layers. Satisfying the interfacial and other necessary boundary conditions on the seafloor and the free surface results in a set of model equations in terms of the interfacial and free surface displacements and the characteristic horizontal velocity components representing each layer.

Thus, following the idea outlined above, the objective of this paper is to present a two-dimensional multi-layer internal wave model in shallow water, which makes no assumption on the size of the wave amplitude. The only approximation used is that the water depth is small in comparison with the horizontal length scale of internal wave motions. The resulting model can deal with large-amplitude non-breaking waves propagating in two horizontal dimensions interacting with various seafloor features. Since the continuous stratification is approximated by a stack of N homogeneous density layers, the model is therefore capable of simulating higher modes up to $N-1$. The depth-integrated two-layer models by Choi (2000) and Lynett & Liu (2002) turn out to be special cases of the present model.

The paper is organized as follows. In §§ 2–4, the approximations and procedures for deriving a set of depth-integrated internal wave equations in a multi-layer fluid system are presented. In §§ 5 and 6, we check the validity of the new model in the weakly nonlinear wave regime by comparing the new numerical results with available data. A numerical algorithm based on the Adams–Bashforth–Moulton predictor–corrector finite difference scheme is proposed in § 5 to numerically solve the governing equations. The numerical results of the proposed model are compared in § 6.1 with the experimental measurements for large-amplitude internal waves in a two-layer fluid system. In § 6,

https://doi.org/10.1017/jfm.2012.24 Published online by Cambridge University Press

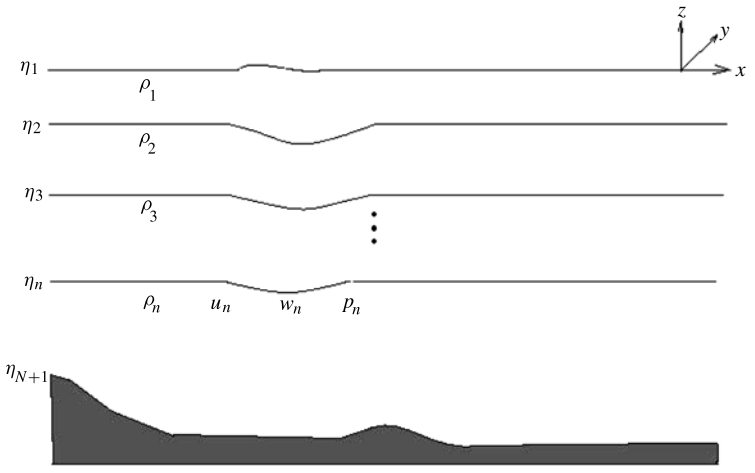


FIGURE 1. Sketch of N-layer fluid system.

numerical studies are performed to demonstrate that the present model can indeed simulate mode-2 internal waves.

2. Governing equations and boundary conditions

In the following derivations, the density stratification in the water column is approximated by N layers. Within each layer, the density remains a constant (see figure 1). By assuming an incompressible inviscid fluid, the flow motions in each layer are described by Euler equations with boundary and interfacial conditions. In the nth layer, the governing equations can be written as

$$\nabla \cdot \boldsymbol{u}_n + w_{nz} = 0, \tag{2.1}$$

$$\boldsymbol{u}_{nt} + \boldsymbol{u}_n \cdot \nabla \boldsymbol{u}_n + w_n \boldsymbol{u}_{nz} = -\frac{1}{\rho_n} \nabla p_n, \tag{2.2}$$

$$w_{nt} + \boldsymbol{u}_n \cdot \nabla w_n + w_n w_{nz} = -\frac{1}{\rho_n} p_{nz} - g, \tag{2.3}$$

where $\nabla = (\partial/\partial x, \partial/\partial y)$ is the horizontal gradient operator; and the subscripts z and t stand for the partial derivatives with respect to z and t, respectively. The coordinate system is chosen so that the plane formed by the x-axis and y-axis coincides with the free surface at rest, with the z-axis pointing upwards. Referring to figure 1, the nth layer is bounded by the upper interface $z = \eta_n$ and the lower interface $z = \eta_{n+1}$. In the bottom layer, the Nth layer, $z = \eta_{N+1}$ describes the seafloor configuration. On the other hand, in the uppermost layer, $z = \eta_1$ denotes the free surface location. Furthermore, $\boldsymbol{u}_n = (u_n, v_n)$ and w_n denote the horizontal velocity components and the vertical velocity component in the nth layer, respectively. Finally, g is the gravitational acceleration, ρ_n is the density, and p_n is the total pressure in the nth layer.

Along the interfaces, free surface and seafloor, kinematic boundary conditions (i.e. these boundaries are material surfaces) must be satisfied. On the other hand, dynamic boundary conditions (continuity of pressure) must be satisfied along the interfaces and free surface. Thus,

$$p_n = p_{n-1} \quad \text{on } z = \eta_n \ (n = 2, \ldots, N), \tag{2.4}$$

https://doi.org/10.1017/jfm.2012.24 Published online by Cambridge University Press

$$w_n = \frac{\partial \eta_n}{\partial t} + \boldsymbol{u}_n \cdot \nabla \eta_n \quad \text{on } z = \eta_n \ (n = 1, \ldots, N), \tag{2.5}$$

$$w_n = \frac{\partial \eta_{n+1}}{\partial t} + \boldsymbol{u}_n \cdot \nabla \eta_{n+1} \quad \text{on } z = \eta_{n+1} \ (n = 1, \ldots, N). \tag{2.6}$$

On the free surface, $z = \eta_1$, the atmospheric pressure, p_a, is assumed to be known. Thus

$$p_1 = p_a \quad \text{at } z = \eta_1. \tag{2.7}$$

Following Choi & Camassa (1999), who developed a rigid-lid two-layer model, we introduce the characteristic length of the wave motion l_0 as the horizontal length scale, the characteristic water depth h_0 as the vertical length scale, ρ_0 as the characteristic density and U_0 as the characteristic velocity. Then the following dimensionless variables can be defined:

$$\begin{gathered}(x, y) = l_0(x', y'), \quad z = h_0 z', \quad t = \frac{l_0}{U_0} t', \quad \eta_n = h_0 \eta_n', \quad \rho_n = \rho_0 \rho_n', \\ h = h_0 h', \quad p_n = \rho_0 U_0^2 p_n', \quad (u_n, v_n) = U_0(u_n', v_n'), \quad w_n = \mu U_0 w_n',\end{gathered} \tag{2.8}$$

in which the prime symbol ($'$) denotes dimensionless quantities. A dimensionless parameter

$$\mu = \frac{h_0}{l_0}, \tag{2.9}$$

representing the ratio of the characteristic water depth, h_0, and the characteristic horizontal length of the wave motion, l_0, has been introduced. In this paper we are interested in internal waves in shallow water and μ is considered to be a small parameter (i.e. $\mu^2 \ll 1$). Here, the total water depth is chosen as the characteristic depth. Hence, we propose to design the multi-layer system in such a way that the density stratification is properly resolved and the layer thicknesses are smaller than the characteristic wavelength of interest.

We reiterate here that, since we have not introduced an additional length scale for the internal wave amplitude, it is implied that the wave amplitude has the same scale as the total water depth. Thus the resulting equations are fully nonlinear.

Using the dimensionless variables, the governing equations and boundary conditions can be rewritten in the following non-dimensional form, with the prime ($'$) now being dropped:

$$\nabla \cdot \boldsymbol{u}_n + w_{nz} = 0, \tag{2.10}$$

$$\boldsymbol{u}_{nt} + \boldsymbol{u}_n \cdot \nabla \boldsymbol{u}_n + w_n \boldsymbol{u}_{nz} = -\frac{1}{\rho_n} \nabla p_n, \tag{2.11}$$

$$\mu^2 \{w_{nt} + \boldsymbol{u}_n \cdot \nabla w_n + w_n w_{nz}\} = -\frac{1}{\rho_n} p_{nz} - \frac{g h_0}{U_0^2}. \tag{2.12}$$

We choose $U_0 = \sqrt{g h_0}$ so that the last term in the vertical momentum equation (2.12) becomes unity. Thus

$$\mu^2 \{w_{nt} + \boldsymbol{u}_n \cdot \nabla w_n + w_n w_{nz}\} = -\frac{1}{\rho_n} p_{nz} - 1. \tag{2.13}$$

The corresponding dimensionless boundary conditions can be expressed as

$$p_1 = p_a \quad \text{on } z = \eta_1, \tag{2.14}$$

https://doi.org/10.1017/jfm.2012.24 Published online by Cambridge University Press

$$p_n = p_{n-1} \quad \text{on } z = \eta_n \ (n = 2, \ldots, N), \tag{2.15}$$

$$w_n = \frac{\partial \eta_n}{\partial t} + \boldsymbol{u}_n \cdot \nabla \eta_n \quad \text{on } z = \eta_n \ (n = 1, \ldots, N), \tag{2.16}$$

$$w_n = \frac{\partial \eta_{n+1}}{\partial t} + \boldsymbol{u}_n \cdot \nabla \eta_{n+1} \quad \text{on } z = \eta_{n+1} \ (n = 1, \ldots, N). \tag{2.17}$$

3. Fully nonlinear multi-layer model equations

With the weak dispersion assumption (i.e. $\mu \ll 1$), the vertical fluid velocity is not as important as the horizontal velocity. The vertical dependence can be removed by layer integration, which will result in a set of two-dimensional horizontal equations in terms of the interfacial and surface elevation and layer-averaged horizontal velocities. These equations are similar to Boussinesq-type equations for surface gravity waves.

Integrating the continuity equation (2.10) within each layer from $z = \eta_{n+1}$ to $z = \eta_n$,

$$\int_{\eta_{n+1}}^{\eta_n} \nabla \cdot \boldsymbol{u}_n \, \mathrm{d}z + \int_{\eta_{n+1}}^{\eta_n} w_z \, \mathrm{d}z = 0, \tag{3.1}$$

and by using the Newton–Leibnitz rule and applying the boundary conditions at $z = \eta_{n+1}$ and $z = \eta_n$, (2.16) and (2.17), the continuity equation can be transformed into

$$\frac{\partial \eta_n}{\partial t} - \frac{\partial \eta_{n+1}}{\partial t} + \nabla \cdot [(\eta_n - \eta_{n+1}) \overline{\boldsymbol{u}}_n] = 0, \tag{3.2}$$

in which the layer-averaged horizontal velocity, $\overline{\boldsymbol{u}}_n$, has been introduced:

$$\overline{\boldsymbol{u}}_n = \frac{1}{\eta_n - \eta_{n+1}} \int_{\eta_{n+1}}^{\eta_n} \boldsymbol{u}_n \, \mathrm{d}z. \tag{3.3}$$

We note that the layer-integrated continuity equation (3.2) is exact.

Using μ^2 as the small parameter, the dimensionless physical variables can be expanded as power series in μ^2,

$$f = \sum_{k=0}^{\infty} \mu^{2k} f^{(k)}, \tag{3.4}$$

where f denotes a set of physical variables (p_n, u_n, v_n, w_n). It is further assumed that the horizontal vorticity components vanish, i.e.

$$\frac{\partial \boldsymbol{u}_n}{\partial z} = \mu^2 \nabla w_n. \tag{3.5}$$

Then, substituting

$$\boldsymbol{u}_n = \sum_{k=0}^{\infty} \mu^{2k} \boldsymbol{u}_n{}^{(k)}, \tag{3.6}$$

$$w_n = \sum_{k=0}^{\infty} \mu^{2k} w_n{}^{(k)}, \tag{3.7}$$

into (3.5) and collecting terms of the same order yields

$$\frac{\partial \boldsymbol{u}_n^{(0)}}{\partial z} = 0, \tag{3.8}$$

$$\frac{\partial \boldsymbol{u}_n^{(1)}}{\partial z} = \nabla w_n^{(0)}. \tag{3.9}$$

https://doi.org/10.1017/jfm.2012.24 Published online by Cambridge University Press

From (3.8) the leading-order horizontal velocity components are independent of the vertical coordinate, i.e.

$$\boldsymbol{u}_n^{(0)} = \boldsymbol{u}_n^{(0)}(x, y, t). \tag{3.10}$$

Now, substituting (3.6) and (3.7) into the continuity equation (2.10) and boundary conditions (2.16) and (2.17), it follows that

$$\nabla \cdot \boldsymbol{u}_n^{(0)} + w_{nz}^{(0)} = 0, \tag{3.11}$$

$$w_n^{(0)} = \frac{\partial \eta_n}{\partial t} + \boldsymbol{u}_n^{(0)} \cdot \nabla \eta_n \quad \text{on } z = \eta_n, \tag{3.12}$$

$$w_n^{(0)} = \frac{\partial \eta_{n+1}}{\partial t} + \boldsymbol{u}_n^{(0)} \cdot \nabla \eta_{n+1} \quad \text{on } z = \eta_{n+1}, \tag{3.13}$$

in which $n = 1, \ldots, N$

Integrating (3.11) from η_{n+1} to z and applying boundary condition (2.17), the leading-order vertical velocity component can be obtained as

$$w_n^{(0)} = -z\nabla \cdot \boldsymbol{u}_n^{(0)} + \nabla \cdot [\boldsymbol{u}_n^{(0)} \eta_{n+1}] + \frac{\partial \eta_{n+1}}{\partial t}. \tag{3.14}$$

By defining

$$S_n^{(0)} = \nabla \cdot \boldsymbol{u}_n^{(0)}, \tag{3.15}$$

$$T_n^{(0)} = -\nabla \cdot [\boldsymbol{u}_n^{(0)} \eta_{n+1}] - \frac{\partial \eta_{n+1}}{\partial t}, \tag{3.16}$$

(3.14) can be rewritten as

$$w_n^{(0)} = -zS_n^{(0)} - T_n^{(0)}. \tag{3.17}$$

The expression for $\boldsymbol{u}_n^{(1)}$ can be obtained by integrating (3.9) from η_{n+1} to z and applying the expression for $w_n^{(0)}$ as

$$\boldsymbol{u}_n^{(1)} = -\tfrac{1}{2}z^2\nabla S_n^{(0)} - z\nabla T_n^{(0)} + \tfrac{1}{2}\eta_{n+1}^2 \nabla S_n^{(0)} + \eta_{n+1}\nabla T_n^{(0)} + \boldsymbol{u}_n^{(1)}(z = \eta_{n+1}), \tag{3.18}$$

which can be rewritten as

$$\boldsymbol{u}_n^{(1)} = -\tfrac{1}{2}z^2\nabla S_n^{(0)} - z\nabla T_n^{(0)} + C_n(x, y, t), \tag{3.19}$$

$$C_n(x, y, t) = \tfrac{1}{2}\eta_{n+1}^2 \nabla S_n^{(0)} + \eta_{n+1}\nabla T_n^{(0)} + \boldsymbol{u}_n^{(1)}(z = \eta_{n+1}). \tag{3.20}$$

Therefore, the expressions for $\boldsymbol{u}_n$ and w_n can be obtained as

$$\boldsymbol{u}_n = \boldsymbol{u}_n^{(0)}(x, y, t) + \mu^2[-\tfrac{1}{2}z^2\nabla S_n^{(0)} - z\nabla T_n^{(0)} + C_n(x, y, t)] + O(\mu^4), \tag{3.21}$$

$$w_n = -zS_n^{(0)} - T_n^{(0)} + O(\mu^2). \tag{3.22}$$

The above two equations can be further rewritten in terms of the layer-averaged horizontal velocity defined in (3.3). To do so, we first integrate (3.21) from η_{n+1} to η_n to obtain

$$\overline{\boldsymbol{u}}_n = \boldsymbol{u}_n^{(0)} + \mu^2[-A_n\nabla S_n^{(0)} - B_n\nabla T_n^{(0)} + C_n(x, y, t)] + O(\mu^4), \tag{3.23}$$

where

$$A_n = \tfrac{1}{6}(\eta_n^2 + \eta_n\eta_{n+1} + \eta_{n+1}^2), \tag{3.24}$$

$$B_n = \tfrac{1}{2}(\eta_n + \eta_{n+1}). \tag{3.25}$$

https://doi.org/10.1017/jfm.2012.24 Published online by Cambridge University Press

Then we subtract (3.23) from (3.21). The horizontal velocity can be obtained in terms of the layer-averaged velocity, $\overline{\boldsymbol{u}}_n$, and the vertical coordinate z. Thus,

$$\boldsymbol{u}_n = \overline{\boldsymbol{u}}_n + \mu^2[(-\tfrac{1}{2}z^2 + A_n)\nabla S_n + (-z + B_n)\nabla T_n] + O(\mu^4), \tag{3.26}$$

where

$$S_n = \nabla \cdot \overline{\boldsymbol{u}}_n, \tag{3.27}$$

$$T_n = -\nabla \cdot [\overline{\boldsymbol{u}}_n \eta_{n+1}] - \frac{\partial \eta_{n+1}}{\partial t}. \tag{3.28}$$

It should be noted that $\boldsymbol{u}_n^{(0)} = \overline{\boldsymbol{u}}_n - O(\mu^2)$ has been used. Finally, w_n can be expressed as

$$w_n = -zS_n - T_n + O(\mu^2). \tag{3.29}$$

To obtain the horizontal momentum equation in terms of $\overline{\boldsymbol{u}}_n$, the expression for pressure p_n needs to be found first, which can be obtained by integrating the vertical momentum equation (2.13) from z to η_n,

$$\frac{1}{\rho_n}\int_z^{\eta_n} p_{nz}\,\mathrm{d}z = -(\eta_n - z) - \mu^2 \int_z^{\eta_n} [w_{nt} + \boldsymbol{u}_n \cdot \nabla w_n + w_n w_{nz}]\,\mathrm{d}z, \tag{3.30}$$

$$\frac{p_n(z)}{\rho_n} = \frac{p_n(z=\eta_n)}{\rho_n} + \eta_n - z + \mu^2\left[\frac{z^2 - \eta_n^2}{2}P_n + (z - \eta_n)R_n\right] + O(\mu^4), \tag{3.31}$$

where

$$P_n = \frac{\partial S_n}{\partial t} + \overline{\boldsymbol{u}}_n \cdot \nabla S_n - S_n^2, \tag{3.32}$$

$$R_n = \frac{\partial T_n}{\partial t} + \overline{\boldsymbol{u}}_n \cdot \nabla T_n - S_n T_n. \tag{3.33}$$

Now, substituting the pressure expression obtained in (3.31) and the expressions for $\boldsymbol{u}_n$ and w_n into the horizontal momentum equation (2.11) and after some algebra, the horizontal momentum equation can be rewritten in terms of the layer-averaged horizontal velocity, $\overline{\boldsymbol{u}}_n$, as

$$\frac{\partial \overline{\boldsymbol{u}}_n}{\partial t} + \overline{\boldsymbol{u}}_n \cdot \nabla \overline{\boldsymbol{u}}_n + \nabla \eta_n + \frac{1}{\rho_n}\nabla p_n(z=\eta_n) + \mu^2 \frac{\partial}{\partial t}\{A_n \nabla S_n + B_n \nabla T_n\}$$
$$+ \mu^2 \nabla \left\{\overline{\boldsymbol{u}}_n \cdot (A_n \nabla S_n + B_n \nabla T_n) + \frac{1}{2}T_n^2 - \frac{\eta_n^2}{2}P_n - \eta_n R_n\right\} = O(\mu^4). \tag{3.34}$$

We note that, in deriving the above equation, the vertical vorticity in each layer is assumed to be weak, i.e. $\nabla \times \overline{\boldsymbol{u}}_n = O(\mu^2)$. Applying the boundary condition (2.15), the term $p_n(z=\eta_n)$ can be expressed as

$$p_n(z=\eta_n) = p_{n-1}(z=\eta_{n-1}) + \rho_{n-1}(\eta_{n-1} - \eta_n)$$
$$+ \mu^2 \rho_{n-1}\left[\frac{\eta_n^2 - \eta_{n-1}^2}{2}P_{n-1} + (\eta_n - \eta_{n-1})R_{n-1}\right] + O(\mu^4). \tag{3.35}$$

In summary, in the N-layer fluid system as described in figure 1, the governing equations can be expressed in terms of the interfacial and free surface elevations, η_n, and the vertically averaged velocity in each layer, $\overline{\boldsymbol{u}}_n$, as shown in the set of continuity equations (3.2) and momentum equations (3.34), while the pressure along the interfaces is given in (3.35).

https://doi.org/10.1017/jfm.2012.24 Published online by Cambridge University Press

It should be noted that, on the free surface, $z = \eta_1$, $p_1 = p_a$, with p_a being the known atmospheric pressure. On the other hand, if the rigid-lid assumption is imposed, then $\eta_1 = 0$, p_a becomes the unknown pressure on the lid. Thus, for this N-layer fluid system, there are always $3N$ unknowns, $\overline{\boldsymbol{u}}_n$ and $\overline{v}_n$ $(n = 1, \ldots, N)$, η_n $(n = 2, \ldots, N)$, p_a or η_1 with $3N$ equations.

From the series expansions (3.26) for the horizontal velocity, and the pressure field (3.31), it is clear that the small parameter μ^2 denotes the non-hydrostatic (frequency dispersion) effects. In other words, the limiting case of $\mu \to 0$ represents the hydrostatic approximation and the resulting wave system is non-dispersive. Since no approximation concerning the wave amplitude has been made in the derivation, the layer-averaged governing equations describe fully nonlinear and weakly dispersive waves evolving in a stratified fluid. The proposed set of equations can be applied to study both surface and internal waves. If only a single layer is considered, $n = 1$, the model equations reduce to the extended Boussinesq-type equations for surface waves (Mei 1989). When $n > 1$ and the rigid-lid approximation is not employed, the derived model equations can be used to analyse the interactions between surface waves and internal waves, providing a possibility to investigate internal waves generated by surface forcing such as ship-generated internal waves. Another advantage of the multi-layer model is its capability of simulating internal waves of higher modes. Theoretically, the N-layer fluid system will be able to study internal waves of up to $(N - 1)$ modes.

4. Discussion of special cases

In the following sections, we discuss several well-known models for different physical processes, which can be deduced from the multi-layer model equations just derived.

4.1. *Nonlinear hydrostatic multi-layer model equations*

When the dispersive effect is completely ignored (i.e. $\mu = 0$), the pressure field becomes hydrostatic. Therefore, the pressure along the upper interface of the nth layer can be written as

$$p_n = p_{n-1} + \rho_{n-1} H_n \quad \text{for } n > 1, \tag{4.1}$$

with $p_1 = p_a$ and $H_n = \eta_n - \eta_{n+1}$, which is the thickness of the nth layer. Moreover, the continuity equation (3.2) and momentum equation (3.34) can be simplified to

$$\frac{\partial H_n}{\partial t} + \nabla \cdot [H_n \overline{\boldsymbol{u}}_n] = 0, \tag{4.2}$$

$$\frac{\partial \overline{\boldsymbol{u}}_n}{\partial t} + \overline{\boldsymbol{u}}_n \cdot \nabla \overline{\boldsymbol{u}}_n + \nabla \eta_n + \frac{1}{\rho_n} \nabla p_n = 0. \tag{4.3}$$

Thus, the nonlinear, hydrostatic, multi-layer equations for stratified flow are recovered (Baines 1995) and are subsets of the general model equations.

4.2. *Shallow water model for surface waves*

Consider a single layer, i.e. $N = 1$. The model equations (4.2) in this case can be further reduced to the nonlinear shallow water equations for surface waves,

$$\frac{\partial H_1}{\partial t} + \nabla \cdot [H_1 \overline{\boldsymbol{u}}_1] = 0, \tag{4.4}$$

https://doi.org/10.1017/jfm.2012.24 Published online by Cambridge University Press

$$\frac{\partial \overline{\boldsymbol{u}}_1}{\partial t} + \overline{\boldsymbol{u}}_1 \cdot \nabla \overline{\boldsymbol{u}}_1 + \nabla \eta_1 = 0, \tag{4.5}$$

where $z = \eta_1$ denotes the free surface location, $z = \eta_2$ the seafloor position and $H_1 = \eta_1 - \eta_2$ the total water depth. Since η_2 can depend on time, the shallow water model thus considers the effects of seafloor motion. Note that the atmospheric pressure, p_a, has been assumed to be a constant.

4.3. *Boussinesq-type models for surface waves*

If the frequency dispersion terms are included for the single-layer system ($N = 1$), the multi-layer model equations (3.2) and (3.34) can be reduced to the fully nonlinear Boussinesq-type equations for surface gravity waves. These model equations agree with those derived by Liu (1994). The expressions are quite lengthy and will not be repeated here.

4.4. *Two-layer internal wave models*

Some of the numerical examples shown in this paper are based on the two-layer model, which is a subset of the general model with $N = 2$. Here we shall discuss the differences and similarities between the present model and other existing models.

The model developed by Lynett & Liu (2002) contains several additional approximations. First, their model is suitable only for weakly nonlinear internal waves with the assumption that $O(\varepsilon^3) = O(\mu^4) \ll 1$, where $\varepsilon = a_0/h_0$. Furthermore, they also assume that the density differences between two layers are small, i.e. $(\rho_2 - \rho_1)/\rho_2 = O(\mu^4)$. If we adopt these additional assumptions in our model equations (3.2) and (3.34), after some lengthy but straightforward manipulations the fully nonlinear multi-layer equations can be reduced to the weakly nonlinear two-layer internal wave model derived by Lynett & Liu (2002).

Assuming a constant water depth, Choi & Camassa (1999) derived a set of equations for fully nonlinear horizontally one-dimensional internal waves in a two-layer fluid system with a rigid-lid approximation. It is straightforward to show that Choi and Camassa's model equations can indeed be deduced from our general model equations.

5. Numerical algorithm for solving the model equations

A numerical algorithm based on the Adams–Bashforth–Moulton predictor–corrector finite differencing method (Wei & Kirby 1995) is employed to find a numerical solution of the multi-layer equations (3.2) and (3.34). For convenience, we first define

$$E = \nabla \cdot [(\eta_n - \eta_{n+1})\overline{\boldsymbol{u}}_n], \tag{5.1}$$

$$F_1 = \overline{u}_n \frac{\partial \overline{u}_n}{\partial x} + \overline{v}_n \frac{\partial \overline{u}_n}{\partial y} + \frac{\partial \eta_n}{\partial x} + \frac{1}{\rho_n} \frac{\partial p_n(z = \eta_n)}{\partial x}, \tag{5.2}$$

$$F_2 = A_n \frac{\partial S_n}{\partial x} + B_n \frac{\partial T_n}{\partial x}, \tag{5.3}$$

$$\begin{aligned} F_3 = {} & \overline{u}_n \frac{\partial F_2}{\partial x} + F_2 \frac{\partial \overline{u}_n}{\partial x} + \overline{v}_n \frac{\partial G_2}{\partial x} + G_2 \frac{\partial \overline{v}_n}{\partial x} + T_n \frac{\partial T_n}{\partial x} \\ & - \eta_n P_n \frac{\partial \eta_n}{\partial x} - \frac{\eta_n^2}{2} \frac{\partial P_n}{\partial x} - \eta_n \frac{\partial R_n}{\partial x} - \frac{\partial \eta_n}{\partial x} R_n, \end{aligned} \tag{5.4}$$

$$F = F_1 + \mu^2 (F_{2t} + F_3), \tag{5.5}$$

$$G_1 = \overline{u}_n \frac{\partial \overline{v}_n}{\partial x} + \overline{v}_n \frac{\partial \overline{v}_n}{\partial y} + \frac{\partial \eta_n}{\partial y} + \frac{1}{\rho_n} \frac{\partial p_n(z = \eta_n)}{\partial y}, \tag{5.6}$$

https://doi.org/10.1017/jfm.2012.24 Published online by Cambridge University Press

$$G_2 = A_n \frac{\partial S_n}{\partial y} + B_n \frac{\partial T_n}{\partial y}, \tag{5.7}$$

$$G_3 = \overline{u}_n \frac{\partial F_2}{\partial y} + F_2 \frac{\partial \overline{u}_n}{\partial y} + \overline{v}_n \frac{\partial G_2}{\partial y} + G_2 \frac{\partial \overline{v}_n}{\partial y} + T_n \frac{\partial T_n}{\partial y} - \eta_n P_n \frac{\partial \eta_n}{\partial y} - \frac{\eta_n^2}{2} \frac{\partial P_n}{\partial y} - \eta_n \frac{\partial R_n}{\partial y} - \frac{\partial \eta_n}{\partial y} R_n, \tag{5.8}$$

$$G = G_1 + \mu^2 (G_{2t} + G_3). \tag{5.9}$$

Then the continuity and momentum equations, (3.2) and (3.34), can be rewritten as

$$\frac{\partial \eta_n}{\partial t} - \frac{\partial \eta_{n+1}}{\partial t} + E = 0, \tag{5.10}$$

$$\frac{\partial \overline{u}_n}{\partial t} + F = 0, \tag{5.11}$$

$$\frac{\partial \overline{v}_n}{\partial t} + G = 0. \tag{5.12}$$

The numerical algorithm adopts a high-order predictor–corrector finite difference method. The time and spatial derivatives are discretized as $t = m\Delta t$, $x = i\Delta x$ and $y = j\Delta y$. For simplicity, $\Delta x = \Delta y$ is used in developing the computer code. The level m refers to the current time level with updated information for all physical variables. The predictor stage employs the third-order explicit Adams–Bashforth scheme, given by

$$(\eta_n)_{i,j}^{m+1} = (\eta_{n+1})_{i,j}^{m+1} + [(\eta_n)_{i,j}^m - (\eta_{n+1})_{i,j}^m] - \frac{\Delta t}{12}\{23E_{i,j}^m - 16E_{i,j}^{m-1} + 5E_{i,j}^{m-2}\}, \tag{5.13}$$

$$(\overline{u}_n)_{i,j}^{m+1} = (\overline{u}_n)_{i,j}^m - \frac{\Delta t}{12}\{23F_{i,j}^m - 16F_{i,j}^{m-1} + 5F_{i,j}^{m-2}\}, \tag{5.14}$$

$$(\overline{v}_n)_{i,j}^{m+1} = (\overline{v}_n)_{i,j}^m - \frac{\Delta t}{12}\{23G_{i,j}^m - 16G_{i,j}^{m-1} + 5G_{i,j}^{m-2}\}. \tag{5.15}$$

Once η_n^{m+1}, $\overline{u}_n^{m+1}$ and $\overline{v}_n^{m+1}$ are predicted, the fourth-order Adams–Moulton scheme is used for iteration. Thus,

$$(\eta_n)_{i,j}^{m+1} = (\eta_{n+1})_{i,j}^{m+1} + [(\eta_n)_{i,j}^m - (\eta_{n+1})_{i,j}^m] - \frac{\Delta t}{24}\{9E_{i,j}^{m+1} + 19E_{i,j}^m - 5E_{i,j}^{m-1} + E_{i,j}^{m-2}\}, \tag{5.16}$$

$$(\overline{u}_n)_{i,j}^{m+1} = (\overline{u}_n)_{i,j}^m - \frac{\Delta t}{24}\{9F_{i,j}^{m+1} + 19F_{i,j}^m - 5F_{i,j}^{m-1} + F_{i,j}^{m-2}\}, \tag{5.17}$$

$$(\overline{v}_n)_{i,j}^{m+1} = (\overline{v}_n)_{i,j}^m - \frac{\Delta t}{24}\{9G_{i,j}^{m+1} + 19G_{i,j}^m - 5G_{i,j}^{m-1} + G_{i,j}^{m-2}\}. \tag{5.18}$$

The evaluation of E and F involves both time and spatial derivatives of $\overline{u}_n$, $\overline{v}_n$, η_n and their combinations. Owing to the appearance of higher-order time and spatial derivatives in the governing equations, up to five time levels are used to resolve the time derivatives to the accuracy of $O(\Delta t^3)$. Similarly, in order to have an accuracy of $O(\Delta x^4)$ in spatial derivatives at a grid point, up to three grids on each side are adopted in taking derivatives. The detailed formulae used for temporal and spatial derivatives can be found in Wang (2008).

https://doi.org/10.1017/jfm.2012.24 Published online by Cambridge University Press

6. Numerical examples

In this section, we demonstrate a wide range of applications of the present model by comparing the present numerical solutions with either experimental data or existing theoretical results for different scenarios.

6.1. *Strongly nonlinear internal waves*

Strongly nonlinear solitary waves have been theoretically studied by Grue *et al.* (1997, 1999) using Euler's equations, and by Miyata (1985, 1988) and Choi & Camassa (1999) using the layer-averaged equations with the rigid-lid approximation.

Grue *et al.* (1999) also carried out a series of laboratory experiments in a flume of a two-layer fluid system with fresh water on the top of salt water. Using the 'dam-break' technique similar to that used by Kao, Pan & Renouard (1985), interfacial solitary waves were generated by removing a vertical gate that retains a volume of fresh water in a reservoir at one end of the flume. By carefully adjusting the size of the fresh water reservoir, a single depression-type internal solitary wave was generated with a designed amplitude. However, a train of dispersive trailing waves was also generated. The width of flume used in the experiments is ~0.50 m. The salt water density was $\rho_2 = 1022$ kg m^{-3} and the lower layer thickness was $h_2 = 0.62$ m. The fresh water of density $\rho_1 = 999.0$ kg m^{-3} was gently filled on top of the lower layer, creating a top layer with a thickness of $h_1 = 0.15$ m. In the experiments both wave profiles and velocity structures in the water column were measured. Velocity fields were directly measured via a particle tracking velocimetry (PTV) method. The snapshots of wave profiles were obtained by converting the time history measurements of the pycnocline with the measured phase speed.

The experimental data are used to validate the present model in the regime of strong nonlinear internal waves. Because it is difficult to simulate the dam-breaking mechanism using depth-integrated models, in the present numerical study we employed the strongly nonlinear solitary wave solution of Miyata (1985, 1988), which was later modified by Choi & Camassa (1999) (hereafter we refer to it as the MCC solution) as input data. For completeness, we outline the procedure for obtaining the MCC solution in a two-layer system as follows. Denoting the interfacial elevation as ξ, the solitary wave solution can be obtained by solving the following nonlinear ordinary differential equation in the moving coordinate $X = x - ct$:

$$(\xi_X)^2 = \left[\frac{3g(\rho_2 - \rho_1)}{c^2(\rho_1 h_1^2 - \rho_2 h_2^2)}\right] \frac{\xi^2(\xi - a_-)(\xi - a_+)}{(\xi - a_*)}, \tag{6.1}$$

in which a_* is expressed as

$$a_* = -\frac{h_1 h_2(\rho_1 h_1 + \rho_2 h_2)}{\rho_1 h_1^2 - \rho_2 h_2^2}, \tag{6.2}$$

and a_- and a_+ are obtained by solving the equation

$$\xi^2 + q_1\xi + q_2 = 0, \tag{6.3}$$

where

$$q_1 = -\frac{c^2}{g} - h_1 + h_2, \tag{6.4}$$

$$q_2 = h_1 h_2 \left(\frac{c^2}{c_0^2} - 1\right), \tag{6.5}$$

https://doi.org/10.1017/jfm.2012.24 Published online by Cambridge University Press

$$\frac{c^2}{c_0^2} = \frac{(h_1 - a)(h_2 + a)}{h_1 h_2 - (c_0^2/g)a}, \tag{6.6}$$

$$c_0^2 = \frac{g h_1 h_2 (\rho_2 - \rho_1)}{\rho_1 h_2 + \rho_2 h_1}, \tag{6.7}$$

c_0 is the linear phase speed and a is the (signed) wave amplitude, which is positive for the elevation wave and negative for the depression wave.

In our numerical simulations, a large-amplitude solitary wave, given by the MCC solution (6.1), is calculated and used as the initial condition. Because the solitary wave represented by the MCC solution is not the exact solution of our model equations given in (3.2) and (3.34), it will evolve into a leading solitary wave and a train of trailing waves. The leading wave, having a larger phase speed due to its larger amplitude, in comparison with the trailing waves, separates itself from the trailing waves at a definite stage of evolution and propagates farther independently as a solitary wave. This leading wave is considered as the solitary wave solution of our fully nonlinear internal wave system and will be compared with the experimental data of Grue *et al.* (1999).

In the numerical simulations, the layer thickness and density set-up are the same as those employed in the experiments. The numerical domain is 300 m long and 6 m wide (roughly, 50 wavelengths by one wavelength) to allow the fully nonlinear solitary wave to develop. The solitary wave profiles from the numerical simulations were then compared to the measurements in figure 2 for solitary waves with $a_0/h_1 = 0.22$, $a_0/h_1 = 0.36$ and $a_0/h_1 = 0.62$, respectively.

As shown in figure 2, the numerical results of the present model agree fairly well with the measurements, with the exception of the case of $a_0/h_1 = 0.36$. In the same figures, the corresponding solutions for the KdV equation are also shown. It is well known that the width of a strongly nonlinear solitary wave is broader than that of the solitary wave of the KdV equations (Turner & Vanden-Broeck 1988; Choi & Camassa 1999; Ostrovsky & Grue 2003). The present model shows a consistent broadening effect in comparison with the KdV solutions as a_0/h_1 increases from 0.22 to 0.62, whereas the measurements for the case $a_0/h_1 = 0.36$ appear to be inconsistent. This suggests that the measurement for $a_0/h_1 = 0.36$ may contain errors. The MCC solutions are also plotted in the same figures and they give very similar profiles to our numerical solutions.

The velocity profiles at the trough (the maximum vertical interfacial displacement) of the solitary wave are also compared between the numerical results and the laboratory measurements. The velocities in the experiments were measured using PTV, while the numerical solutions are obtained from (3.26) in terms of the layer-averaged velocity, $\overline{u}_n$, and the vertical coordinate z. The velocity comparisons are shown in figure 3 for $a_0/h_1 = 0.22$, 0.36 and 0.78, respectively. Overall, the agreement is reasonably good. From the experimental data, the sharp velocity gradient across the pycnocline can be easily observed, which provides some support for the model assumption that the velocity is discontinuous across interfaces.

The phase velocities were also indirectly measured by Grue *et al.* (1999) in their experiments. In this study, the phase velocities are also calculated from the numerical simulations for the cases of $a_0/h_1 = 0.22$, 0.36, 0.62 and 0.78, and are compared with the measurements in figure 4. Phase velocities from the weakly nonlinear KdV solution and the strongly nonlinear (MCC) solution (6.6) are also shown in the figure. Obviously, the KdV model is only accurate for small a_0/h_1 values (i.e. weakly nonlinear waves). The discrepancy between the KdV solution and

https://doi.org/10.1017/jfm.2012.24 Published online by Cambridge University Press

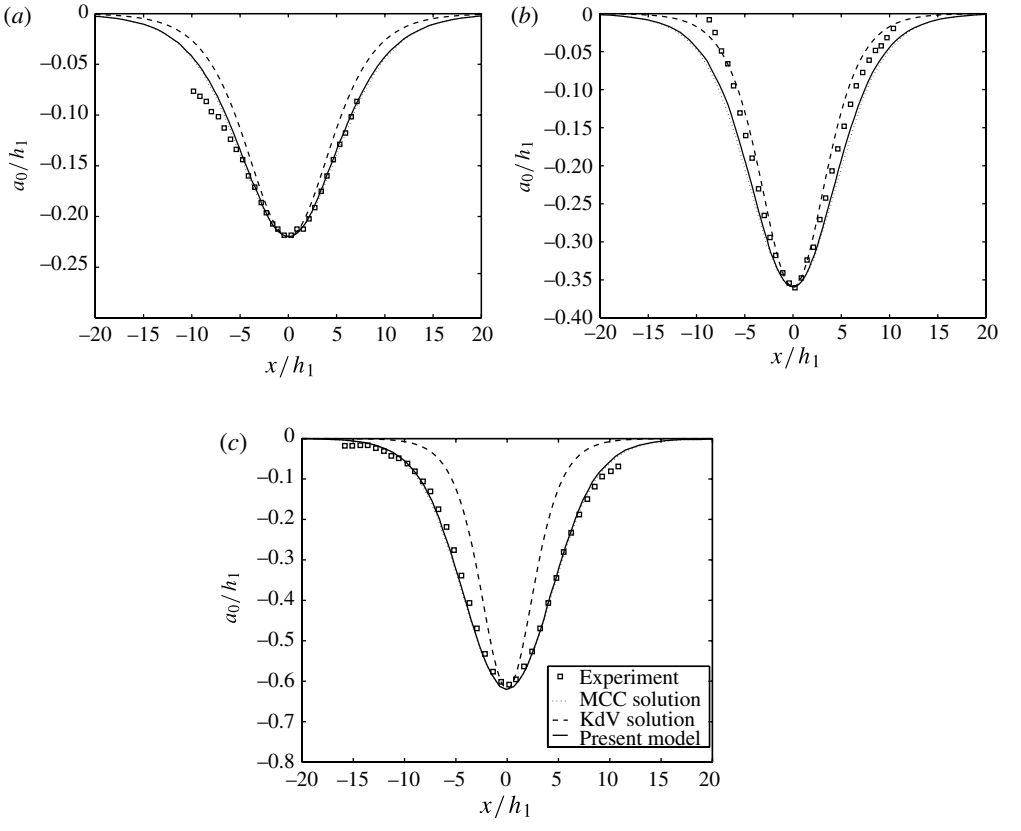


FIGURE 2. Comparison of solitary wave profile between the numerical results and laboratory measurements for (*a*) $a_0/h_1 = 0.22$, (*b*) $a_0/h_1 = 0.36$ and (*c*) $a_0/h_1 = 0.62$. The key applies to all three panels.

strongly nonlinear solutions increases as the wave amplitude becomes larger. The phase velocities obtained from the present numerical model have an almost perfect match with the strongly nonlinear MCC solution.

6.2. *Mode-2 internal waves in a multi-layer fluid system*

In this section, we will demonstrate the application of the present multi-layer model in simulating mode-2 internal waves.

6.2.1. *Generation of mode-2 internal wave via initial isopycnal anomaly*

In the first example, we show that the multi-layer model can simulate a mode-2 internal wave propagating in shallow water, which is generated by an initial isopycnal anomaly. To this end, we specify the density stratification as

$$\rho = \rho_0 - \rho_b(z), \tag{6.8}$$

$$\rho_b(z) = \frac{\Delta\rho}{2}\left[1 + \tanh\left(\frac{z - z_0}{d}\right)\right], \tag{6.9}$$

where ρ_0 is the reference seawater density, $\rho_0 = 1022$ kg m^{-3}, and ρ_b is the stable background stratification. Following Chao *et al.* (2006), we specify the water depth as 300 m, $\Delta\rho = 6$ kg m^{-3}, $z_0 = -80$ m and $d = 120$ m. The density stratification and

https://doi.org/10.1017/jfm.2012.24 Published online by Cambridge University Press

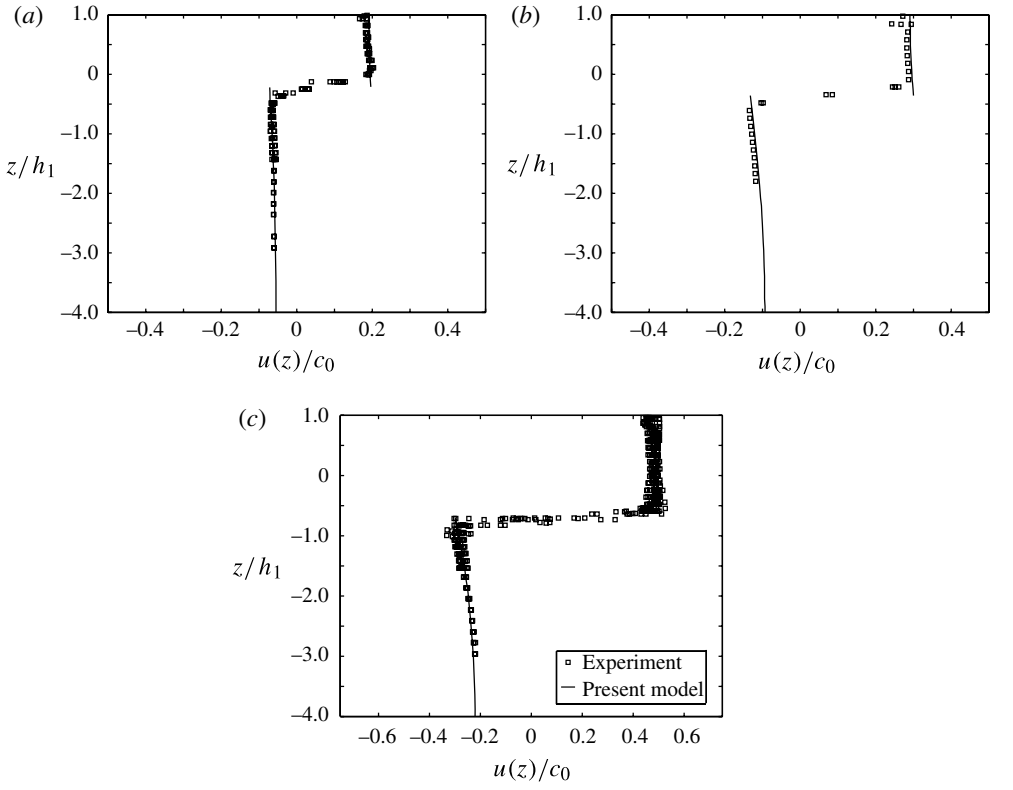


FIGURE 3. Comparison of velocity profile between the numerical results and laboratory measurements for (*a*) $a_0/h_1 = 0.22$, (*b*) $a_0/h_1 = 0.36$ and (*c*) $a_0/h_1 = 0.78$. The key applies to all three panels.

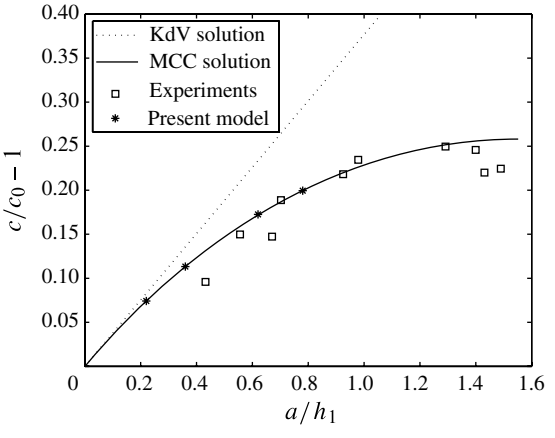


FIGURE 4. Comparison of phase velocities. The MCC solution represents the strongly nonlinear solution given by (6.6).

the corresponding normalized modal structure, $\phi(z)$, of mode-2 waves are shown in figure 5.

https://doi.org/10.1017/jfm.2012.24 Published online by Cambridge University Press

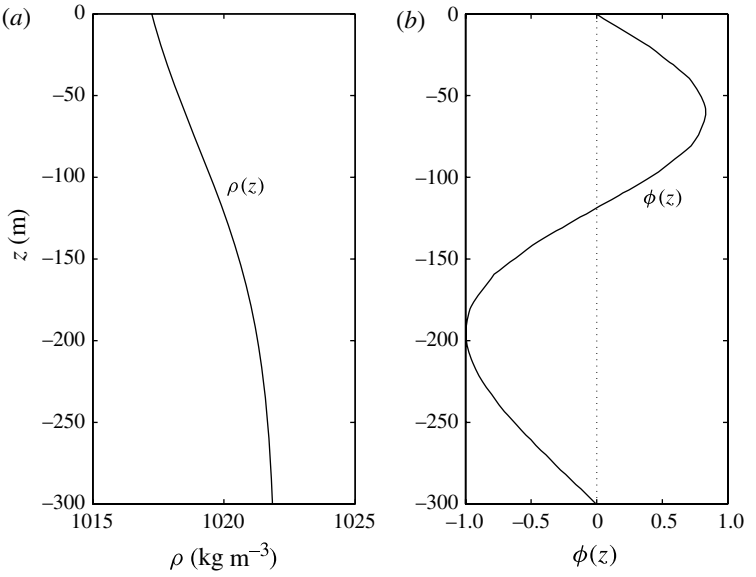


FIGURE 5. Density profile and modal structure of mode-2 internal waves: (*a*) the background density stratification in water column; and (*b*) the normalized modal structure, $\phi(z)$, for mode 2.

Layer no.	Layer thickness (m)	Density (kg m^{-3})
1	30.4	1017.539
2	25.3	1018.114
3	23.3	1018.689
4	23.2	1019.264
5	25.1	1019.839
6	29.8	1020.413
7	42.0	1020.988
8	100.9	1021.563

TABLE 1. Configuration of the multi-layer system for mode-2 study.

The continuous density stratification, shown in figure 5, is approximated by a stair-step profile with eight layers. We recall that the nth layer is bounded by two interfaces, $z = z_n$ and $z = z_{n+1}$. Within each layer, the density is a constant, and the constant density difference between two adjacent layers is 0.575 kg m^{-3}. The density and layer thickness for each layer are given in table 1.

The numerical domain is 80 km long in the x-direction, 4 km wide in the y-direction and 300 m in the vertical direction. The no-flux condition is implemented along all four lateral boundaries. Initial interfacial displacements are introduced on the vertical plane, and the density is uniform in the y-direction. Adopting the mode-2 modal structure $\phi(z)$, given in figure 5, the interfacial displacements are prescribed as

$$\eta_n = a_0 F(x)\phi(z = z_n), \quad n = 1, \ldots, N+1, \tag{6.10}$$

https://doi.org/10.1017/jfm.2012.24 Published online by Cambridge University Press

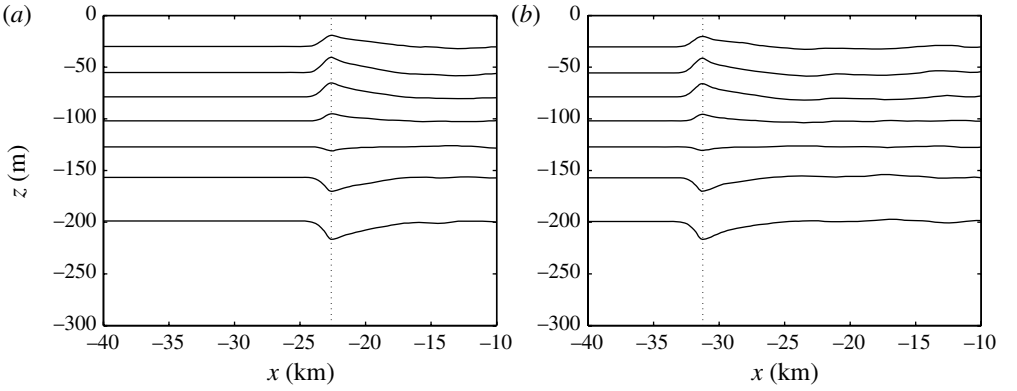


FIGURE 6. Snapshots of interfacial displacements at (*a*) $t = 10$ h and (*b*) $t = 14$ h of propagation. The dotted line marks the peak of the displacements. The amplitudes of the interfacial displacements are doubled in both snapshots for easier viewing.

where a_0 is the characteristic amplitude of interfacial displacements, and $F(x)$ describes the longitudinal profile of initial interfacial displacements, given by

$$F(x) = \begin{cases} 1, & |x| \leqslant L, \\ \mathrm{e}^{-(x+L)^2/2r_0^2}, & x < -L, \\ \mathrm{e}^{-(x-L)^2/2r_0^2}, & x > L, \end{cases} \tag{6.11}$$

where $2L$ denotes the width of the density anomaly. The density discontinuities are smoothed out at both ends of the density anomaly. The initial velocity is assumed to be zero. To carry out numerical computations, the following numerical values are employed: $a_0 = 10$ m, $L = 2.0$ km and $r_0 = 0.5$ km.

The initial interfacial displacement creates an imbalance between gravity and buoyancy. Once released, the upper dome of the initial displacement (i.e. the elevation) will collapse downwards and the lower dome of the initial displacement (i.e. the depression) will move upwards. The potential energy is converted to kinetic energy, and, as a result, the initial interfacial displacement will split into two mode-2 internal waves propagating in opposite directions.

Figure 6(*a*,*b*), respectively, shows snapshots of the internal wave profile after 10 and 14 h propagation. After 10 h propagation, the peak of the leading wave arrives at $x_1 = -22.61$ km (dotted line in figure 6*a*) and after 14 h, the peak reaches $x_2 = -31.25$ km (dotted line in figure 6*b*). The phase velocity can be calculated as $c = (x_1 - x_2)/(4 \times 3600) = 0.60$ m s^{-1}, which is very close to the theoretical linear phase speed 0.58 m s^{-1} of mode-2 waves.

The vertical structure of interfacial displacements is shown in figure 7 and is compared with the theoretical modal structure shown in figure 5. The vertical displacements have been normalized by the maximum value. The results at $t = 10$ h and $t = 14$ h are shown. Very good agreements are obtained.

6.2.2. *Generation of mode-2 waves via interaction with bottom topography*

Mode-2 internal waves can also be generated through interactions between mode-1 internal waves and topographical features, such as a seamount or a break in the continental shelf. In this section, we demonstrate that the multi-layer model can be used to simulate this mode-2 wave generation mechanism. The numerical domain is

https://doi.org/10.1017/jfm.2012.24 Published online by Cambridge University Press

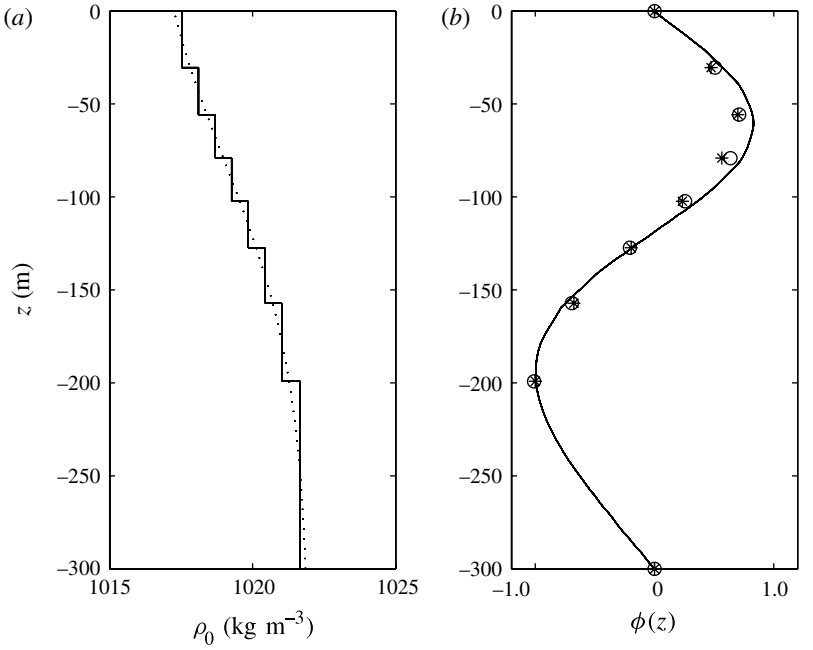


FIGURE 7. (*a*) The density stratification of the eight-layer system and (*b*) the calculated modal structure of the isopycnal displacements. The displacements along the dotted line ($x = -31.25$ km) are first normalized by the maximum displacement and then compared to the theoretical modal structure of a mode-2 wave with the given density stratification. The stars indicate the modal structure of the snapshot at $t = 14$ h and the circles denotes the modal structure of the snapshot at $t = 10$ h.

a channel with water depth of 15 cm. The density stratification is determined by the following three-parameter function for the Brunt–Väisälä frequency:

$$N(z) = N_{max}\left(\left[\frac{2(z+H_p)}{\Delta H_p}\right]^2 + 1\right), \tag{6.12}$$

in which H_p denotes the depth where the Brunt–Väisälä frequency reaches its minimum and ΔH_p is a vertical length scale of the variation of $N(z)$. In the numerical simulations, $N_{max} = 3.95$ s^{-1}, $H_p = 0.112$ m and $\Delta H_p = 0.02$ m are used. The corresponding modal structures of mode-1 and mode-2 internal waves, $\phi_1(z)$ and $\phi_2(z)$, can be calculated using the KdV equation with continuous stratification (Vlasenko & Hutter 2001) (see figure 8). We note that the density stratification employed here is the same as that in the experimental and numerical studies by Huttemann & Hutter (2001) and Vlasenko & Hutter (2001), respectively.

In the numerical simulation, the water depth is divided into eight layers. The locations of undisturbed interfaces, z_n ($n = 1, \ldots, 9$), are given in table 2. Within each layer, the density is constant. The density and thickness for each layer are given in table 3.

The one-dimensional wave channel is 30 m long (from $x = -15.0$ m to $x = 15.0$ m) and 15 cm deep (see figure 9). Sponge layers are applied at both ends of the wave channel to eliminate wave reflections. A uniform grid with $\Delta x = 0.04$ m is used. On the bottom of the channel, a ridge given by the following Gaussian function is placed

https://doi.org/10.1017/jfm.2012.24 Published online by Cambridge University Press

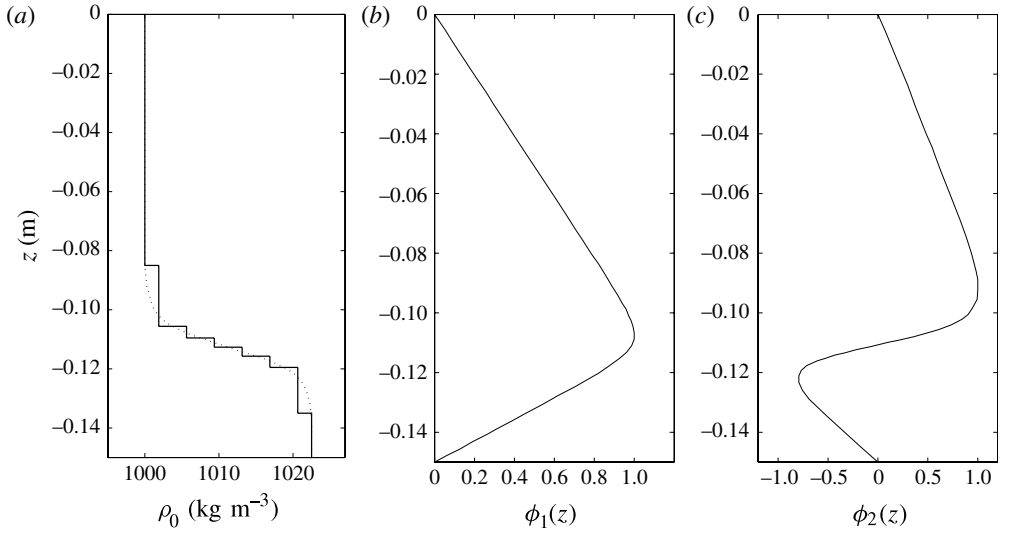


FIGURE 8. (*a*) The continuous density profile (dotted line) and the density profile approximated by an eight-layer fluid system (solid line). The vertical structures of isopycnal displacements corresponding to the continuous density stratification are also given for (*b*) the mode-1 and (*c*) the mode-2 internal waves.

n	1	2	3	4	5
z_n (m)	0.0	−0.085	−0.105 59	−0.109 54	−0.112 66
n	6	7	8	9	
z_n (m)	−0.115 70	−0.119 51	−0.135 00	−0.15	

TABLE 2. Coordinates of layer interfaces.

at $x = 7.5$ m:

$$B(x) = B_0 \mathrm{e}^{-(x-x_0)^2/2r_0^2} - 0.15, \tag{6.13}$$

where $B_0 = 0.028$ m, $x_0 = 7.5$ m and $r_0 = 0.1$ m.

To generate a mode-1 internal wave, the interfaces, η_n ($n = 1, \ldots, 9$), are initially deformed according to the following function:

$$\eta_n = a_0 \phi_1(z_n) S(x, z_n), \quad n = 1, \ldots, 9, \tag{6.14}$$

where a_0 denotes the amplitude ($a_0 = 10$ mm), $\phi_1(z)$ is the vertical profile of interfacial displacements given in figure 8, and $S(x, z_n)$ represents the analytical solution of the mode-1 solitary wave obtained from the KdV equation (Vlasenko 1994; Vlasenko & Hutter 2001). The initial interfacial displacements are shown in figure 9.

Once released, the initial interfacial deformation collapses and separates into two wave packages, travelling in opposite directions; each wave package has an elevation-type leading wave with mode-1 solitary wave profile, which is followed by a

https://doi.org/10.1017/jfm.2012.24 Published online by Cambridge University Press

Layer no.	Layer thickness (m)	Density (kg m^{-3})
1	0.085 00	1000.000
2	0.015 59	1001.875
3	0.003 95	1005.625
4	0.003 12	1009.375
5	0.003 04	1013.125
6	0.003 81	1016.875
7	0.015 49	1020.625
8	0.015 00	1022.500

TABLE 3. Configuration of the eight-layer system for studying mode-2 internal waves.

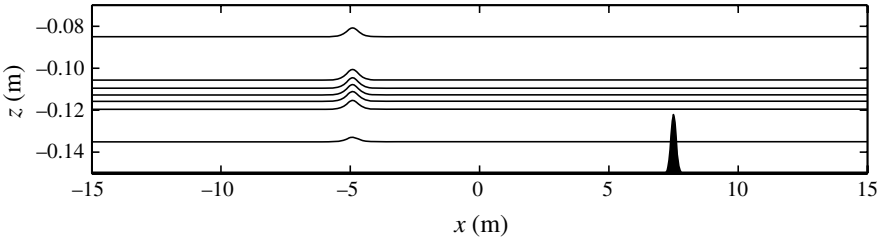


FIGURE 9. The initial displacement of isopycnals and the ridge configuration. The initial isopycnal displacements are calculated according to (6.14) and the ridge is described by (6.13).

train of small-amplitude waves. The right-going leading wave, with amplitude of $a_0 = 4.9$ mm, travels over a distance of 10 m before encountering the underwater ridge (see figure 10). The phase speed of the leading wave is determined numerically as $c_{01} = 0.072$ m s^{-1}, which is very close to the theoretical estimation based on the KdV equation (0.071 m s^{-1}).

Figure 10 shows snapshots of interfacial deformations when the mode-1 internal waves interact with the bottom ridge at different phases. As seen in the figure, a couple of interfaces intersect with the ridge during the process. A moving boundary scheme, similar to the one developed by Lynett, Wu & Liu (2002), has been employed in the present model.

From the snapshots, it is clear that, as the mode-1 incident internal wave encounters the bottom ridge, most of the wave energy is transmitted over the ridge (figure 10*d*,*e*). The isopycnals of the transmitted wave show co-phase displacements of elevation type throughout the entire depth. As shown in figure 11(*a*,*b*), we find that the vertical distributions of isopycnal displacements and the horizontal velocity of the transmitted wave are in good agreement with those derived from the KdV solutions for the mode-1 solitary wave of the same amplitude (4.2 mm).

Figure 10(*e*) indicates that a second transmitted wave appears at around $x = 8.6$ m, trailing the first one. The amplitude of the second transmitted wave is $\sim$1.0 mm, much smaller than that of the first transmitted wave (4.2 mm). The second transmitted wave displays qualitatively a mode-2 profile of isopycnal deformations. In figure 11(*c*,*d*), detailed comparisons of the vertical distribution of horizontal velocities and interfacial displacements show very good agreement with the analytical solutions of the

https://doi.org/10.1017/jfm.2012.24 Published online by Cambridge University Press

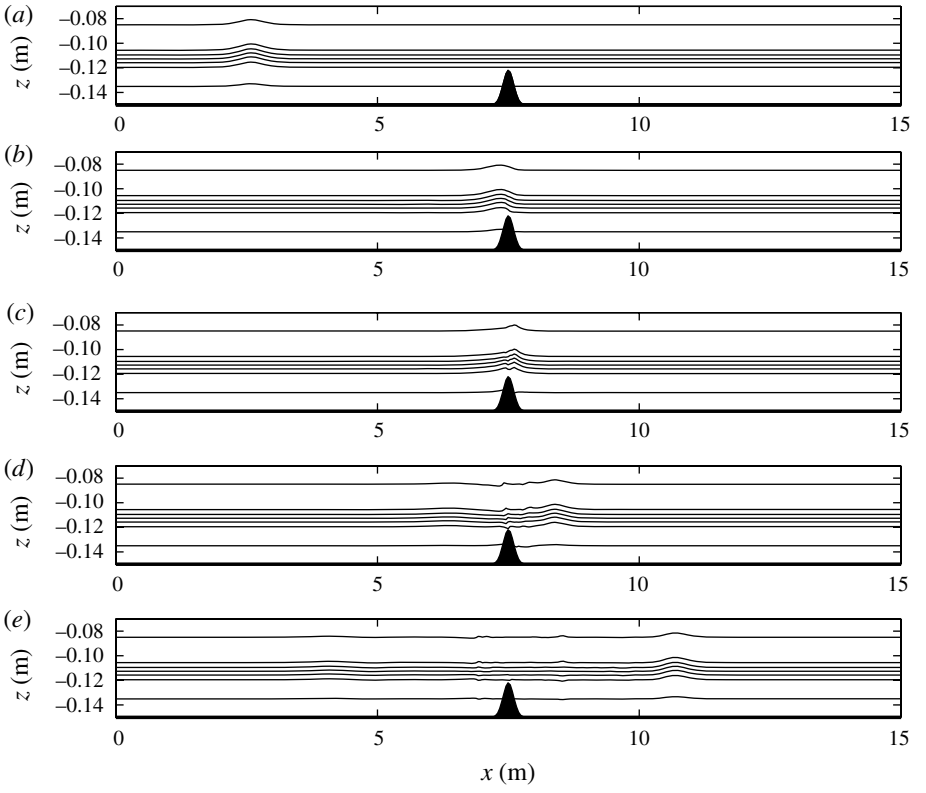


FIGURE 10. Snapshots of interfacial profiles when the internal wave is approaching, interacting with, and passing over the ridge. The panels show the first and second transmitted/reflected internal waves.

KdV equation (Vlasenko & Hutter 2001). The phase speed of the second transmitted internal wave is numerically estimated at $\sim$0.020 m s^{-1}, which is very close to the theoretical value of 0.021 m s^{-1} given by KdV solitary wave solution.

Besides the mode-1 and mode-2 transmitted internal waves, two reflected internal waves are also observed, corresponding to the first and second transmitted waves. However, they are not very prominent, owing to their small amplitudes and the disturbance on background stratification. The first reflected wave, with an amplitude of $\sim$1.1 mm, shows characteristics of the mode-1 internal wave. Figure 12 illustrates the structure of (*a*) the interfacial displacements and (*b*) the horizontal velocity of the first reflected wave. The agreement between the numerical results and the analytical solution is very reasonable.

Figure 12 also displays the vertical structures of interfacial displacements and velocity of the second reflected wave, which is associated with the second transmitted internal wave and has an amplitude of $\sim$0.8 mm. The comparison with the analytical solution is also made, but the difference is large compared to that of the second transmitted internal wave (figure 12*c*,*d*). This is probably because the second reflected wave propagates over a background stratification highly disturbed by the transmitted waves and the first reflected wave.

https://doi.org/10.1017/jfm.2012.24 Published online by Cambridge University Press

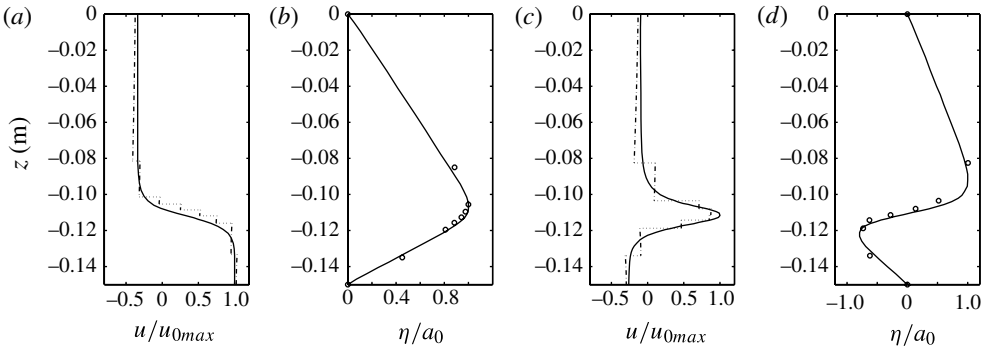


FIGURE 11. The vertical structures of the isopycnal displacements and the horizontal velocities of the first and second transmitted waves shown in figure 10(*e*). The isopycnal displacements are normalized by the maximum amplitude ($a_0 = 4.2$ mm for the first transmitted wave and $a_0 = 1.0$ mm for the second transmitted wave). The horizontal velocities are normalized by the maximum value determined from the KdV solution. The dashed-dotted line shows the numerical results and the solid line denotes the KdV solution of the same amplitude. (*a*,*b*) The comparison for the first transmitted wave and (*c*,*d*) the comparison for the second transmitted wave.

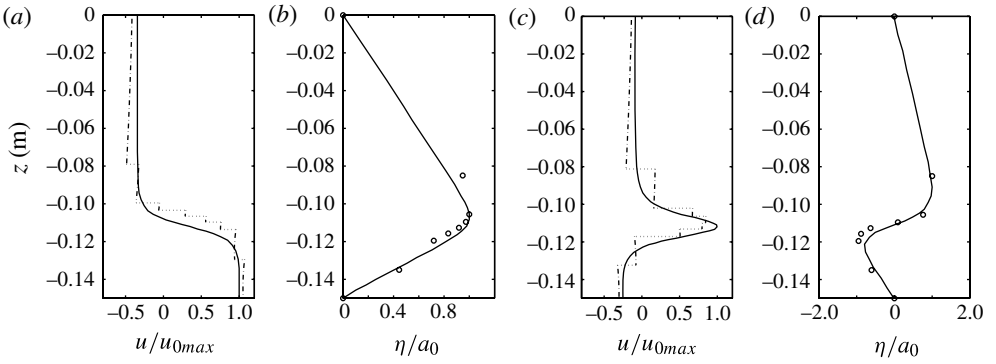


FIGURE 12. The vertical structures of the isopycnal displacements and the horizontal velocities of the first and second reflected waves shown in figure 10(*e*). The isopycnal displacements are normalized by the maximum amplitude ($a_0 = 1.1$ mm for the first reflected wave and $a_0 = 0.8$ mm for the second reflected wave). The horizontal velocities are normalized by the maximum value determined from the KdV solution. The dashed-dotted line shows the numerical results and the solid line denotes the KdV solution of the same amplitude. (*a*,*b*) The comparison for the first reflected wave and (*c*,*d*) the comparison for the second reflected wave.

7. Concluding remarks

In this paper, a multi-layer internal wave model has been developed, in which a stack of N constant-density layers is used to approximate continuous stratification. The model assumes that the wavelength of interest is long in comparison with the total water depth. The magnitude of wave amplitude is arbitrary as long as waves do not break. Thus, the model is capable of describing finite-amplitude, weakly dispersive internal waves up to breaking. However, the model is restricted by the requirement that the vertical vorticity component must vanish and the horizontal vorticity components

https://doi.org/10.1017/jfm.2012.24 Published online by Cambridge University Press

are weak. In a series of numerical experiments, we have demonstrated that the present model can simulate both weakly and strongly nonlinear mode-1 internal wave evolution. In these cases, both nonlinear and dispersive effects are important and need to be included in the model. The numerical results show very good agreement with experimental data. It is clear that the KdV equation model, which allows only weakly nonlinear waves, produces less satisfactory results. We have also shown that, since the multi-layer model can simulate continuous stratification, the model is capable of describing the generation of mode-2 internal waves through the interaction between mode-1 waves with a sea ridge. Further efforts need to be made to implement the model to study the horizontally two-dimensional evolutions of internal waves in field conditions. It would also be interesting to include the Coriolis forces in the future model equation and investigate their effects.

Acknowledgements

The research work presented here is supported by grants from the National Science Foundation to Cornell University.

REFERENCES

APEL, J. R., BADIEY, M., CHIU, C.-S., FINETTE, S., HEADRICK, R., KEMP, J., LYNCH, J. F., NEWHALL, A., ORR, M. H., PASEWARK, B. H., TIELBUERGER, D., TURGUT, A., VON DER HEYDT, K. & WOLF, S. 1997 An overview of the 1995 SWARM shallow-water internal wave acoustic scattering experiment. *IEEE J. Ocean. Engng* **22**, 465–500.

BAINES, P. G. 1995 *Topographic Effects in Stratified Flows*. Cambridge University Press.

BOLE, J. B., EBBESMEYER, C. C. & ROMEA, R. D. 1994 Soliton currents in the South China Sea: measurements and theoretical modelling. In *Proceedings of the 26th Annual Offshore Technology Conference, Houston, TX*, 1994, pp. 367–376.

CAMASSA, R., CHOI, W., MICHALLET, H., RUSAS, R.-O. & SVEEN, J. K. 2006 On the realm of validity of strongly nonlinear asymptotic approximations for internal waves. *J. Fluid Mech.* **549**, 1–23.

CHAO, S.-Y., SHAW, P.-T., HSU, M.-K. & YANG, Y.-J. 2006 Reflection and diffraction of internal solitary waves by a circular island. *J. Oceanogr.* **62**, 811–823.

CHEN, Y. & LIU, P. L.-F. 1995 The unified Kadomtsev–Petviashvili equation for interfacial waves. *J. Fluid Mech.* **288**, 383–408.

CHOI, W. 2000 Modeling of strongly nonlinear internal gravity waves. In *Proceedings of 4th International Conference on Hydrodynamics, Yokohama, Japan*, pp. 453–458.

CHOI, W. & CAMASSA, R. 1996 Weakly nonlinear internal waves in a two-fluid system. *J. Fluid Mech.* **313**, 83–103.

CHOI, W. & CAMASSA, R. 1999 Fully nonlinear internal waves in a two-fluid system. *J. Fluid Mech.* **396**, 1–36.

DAVIS, R. E. & ACRIVOS, A. 1967 Solitary internal waves in deep water. *J. Fluid Mech.* **29**, 593–607.

DEBSARMA, S., DAS, K. P. & KIRBY, J. T. 2010 Fully nonlinear higher-order model equations for long internal waves in a two-fluid system. *J. Fluid Mech.* **654**, 281–303.

DUDA, T. F., LYNCH, J. F., IRISH, J. D., BEARDSLEY, R. C., RAMP, S.R., CHIU, C.-S., TANG, T. Y. & YANG, Y.-J. 2004 Internal tide and nonlinear wave behavior in the continental slope in the northern South China Sea. *IEEE J. Ocean. Engng* **29**, 1105–1131.

EVANS, W. A. & FORD, M. J. 1996 An integral equations approach to internal (two-layer) solitary waves. *Phys. Fluids* **8**, 2032–2047.

FARMER, D. M. 1978 Observations of long nonlinear internal waves in a lake. *J. Phys. Oceanogr.* **8**, 63–73.

GRIMSHAW, R., PELINOVSKY, E. & PLOUKHINA, O. 2002 Higher-order Korteweg–de Vries models for internal solitary waves in a stratified shear flow with a free surface. *Nonlinear Process. Geophys.* **9**, 221–235.

https://doi.org/10.1017/jfm.2012.24 Published online by Cambridge University Press

GRUE, J., FRIIS, H. A., PALM, E. & RUSAS, P.-O. 1997 A method for computing unsteady fully nonlinear interfacial waves. *J. Fluid Mech.* **351**, 223–252.

GRUE, J., JENSEN, A. & RUSAS, P.-O. 1999 Properties of large-amplitude internal solitary waves. *J. Fluid Mech.* **413**, 181–217.

HELFRICH, K. R. 1992 Internal solitary waves breaking and run-up on a uniform slope. *J. Fluid Mech.* **243**, 133–154.

HSU, M.-K., LIU, A. K. & LIU, C. 2000 A study of internal waves in the China Seas and Yellow Sea using SAR. *Cont. Shelf Res.* **20**, 389–410.

HUTTEMANN, H. & HUTTER, K. 2001 Baroclinic solitary water waves in a two-layered fluid with diffusive interface. *Exp. Fluids* **30**, 317–326.

JO, T.-C. & CHOI, W. 2002 Dynamics of strongly nonlinear solitary waves in the shallow water. *Stud. Appl. Maths* **109**, 205–227.

KAO, T. W., PAN, F.-S. & RENOUARD, D. 1985 Internal soliton on pycnocline: generation, propagation, and shoaling and breaking over slope. *J. Fluid Mech.* **159**, 1965–1985.

KAO, T. W. & PAO, H.-P. 1980 Wave collapse in the thermocline and internal solitary waves. *J. Fluid Mech.* **97**, 116–127.

LAMB, K. G. 2000 Conjugate flows for a three-layer fluid. *Phys. Fluids* **12** (9), 2169–2185.

LEE, C.-Y. & BEARDSLEY, R. C. 1974 The generation of long nonlinear internal waves in a weakly stratified shear flow. *J. Geophys. Res.* **79**, 453–462.

LIU, A. K. 1988 Analysis of nonlinear internal waves in the New York Bight. *J. Geophys. Res.* **93**, 122–317.

LIU, A. K., CHANG, Y. S., HSU, M.-K. & LIANG, N. K. 1998 Evolution of nonlinear internal waves in the East and South China Seas. *J. Geophys. Res.* **103**, 7995–8008.

LIU, P. L.-F. 1994 Model equations for wave propagations from deep to shallow water. *Adv. Coast. Ocean Engrg.* **1**, 125–158.

LYNETT, P. & LIU, P. L.-F. 2002 A two-dimensional, depth-integrated model for internal wave propagation over variable bathymetry. *Wave Motion* **36**, 221–240.

LYNETT, P., WU, T.-R. & LIU, P. L.-F. 2002 Modeling wave runup with depth-integrated equations. *Coast. Engng* **46**, 89–107.

MAXWORTHY, T. 1980 On the formation of nonlinear internal waves from the gravitational collapse of mixed regions in two and three dimensions. *J. Fluid Mech.* **96**, 47–64.

MAXWORTHY, T. 1983 Experiments on solitary internal Kelvin waves. *J. Fluid Mech.* **129**, 365–383.

MEI, C. C. 1989 *The Applied Dynamics of Ocean Surface Waves*. World Scientific.

MICHALLET, H. & BARTHELEMY, E. 1998 Experimental study of interfacial solitary waves. *J. Fluid Mech.* **206**, 159–177.

MIYATA, M. 1985 An internal solitary wave of large amplitude. *La Mer* **23**, 43–48.

MIYATA, M. 1988 Long internal waves of large ampliude. In *Nonlinear Water Waves, IUTAM Symposium, Tokyo 1987* (ed. K Horikawa & H Maruo), pp. 399–406. Springer.

OSTROVSKY, L. A. & GRUE, J. 2003 Evolution equations for strongly nonlinear internal waves. *Phys. Fluids* **15**, 2934–2948.

RUSAS, P.-O. & GRUE, J. 2002 Solitary waves and conjugate flows in a three-layer fluid. *Eur. J. Mech.* B/*Fluids* **21**, 185–206.

SAFFARINIA, K. & KAO, T. W. 1996 A numerical study of the breaking of internal soliton and its interaction with a slope. *Dyn. Atmos. Oceans* **23** (1/4), 379–391.

SANDSTROM, H. & ELLIOT, J. A. 1984 Internal tide and solitons on the Scotian shelf: a nutrient pump at work. *J. Geophys. Res.* **89** (4), 6415–6426.

SMALL, J. 2001*a* A nonlinear model of the shoaling and refraction of interfacial solitary waves in the ocean. Part I. Development of the model and investigations of the shoaling effect. *J. Phys. Oceanogr.* **31**, 3163–3183.

SMALL, J. 2001*b* A nonlinear model of the shoaling and refraction of interfacial solitary waves in the ocean. Part II. Oblique refraction across a continental slope and propagation over a seamount. *J. Phys. Oceanogr.* **31**, 3184–3199.

STAMP, A. P. & JACKA, M. 1995 Deep-water internal solitary waves. *J. Fluid Mech.* **305**, 347–371.

STANTON, T. P. & OSTROVSKY, L. A. 1998 Observations of highly nonlinear solitons over continental shelf. *Geophys. Res. Lett.* **25**, 2695–2698.

https://doi.org/10.1017/jfm.2012.24 Published online by Cambridge University Press

TEREZ, D. E. & KNIO, O. M. 1998 Numerical simulations of large-amplitude internal solitary waves. *J. Fluid Mech.* **362**, 53–82.

TOMASSON, G. & MELVILLE, W. 1992 Geostrophic adjustment in a channel: nonlinear and dispersive effects. *J. Fluid Mech.* **241**, 23–57.

TURNER, R. E. L. & VANDEN-BROECK, J.-M. 1988 Broadening of interfacial solitary waves. *Phys. Fluids* **31**, 2486–2491.

VAZQUEZ, A., STASHCHUK, N., VLASENKO, V., BRUNO, M., IZQUIERDO, A. & GALLACHER, P. C. 2006 Evidence of multimodal structure of the baroclinic tide in the Strait of Gibraltar. *Geophys. Res. Lett.* **33**, L17605.

VLASENKO, V. I. 1994 Multi-modal soliton of internal waves. *Atmos. Ocean. Phys.* **30**, 161–169.

VLASENKO, V. I. & ALPERS, W. 2005 Generation of secondary internal waves by the interaction of an internal solitary wave with an underwater bank. *J. Geophys. Res.* **110**, C02019.

VLASENKO, V. I. & HUTTER, K. 2001 Generation of second mode solitary waves by the interaction of a first model soliton with a sill. *Nonlinear Process. Geophys.* **8**, 223–239.

WANG, X. 2008 Numerical modelling of surface and internal waves over shallow and intermediate water. PhD Thesis, Cornell University.

WEI, G. & KIRBY, J. T. 1995 A time-dependent numerical code for extended Boussinesq equations. *J. Waterways Port Coast. Engrg* **121**, 251–261.

YANG, Y.-J., TANG, T. Y., CHANG, M. H., LIU, A. K., HSU, M.-K. & RAMP, S. 2004 Solitons northeast of Tung-Sha Island during the ASIAEX pilot studies. *IEEE J. Ocean. Engng* **29** (4), 1182–1199.

https://doi.org/10.1017/jfm.2012.24 Published online by Cambridge University Press